

Exposure Completing for Temporally Consistent Neural High Dynamic Range Video Rendering

Jiahao Cui
School of AIA, Huazhong University
of Science and Technology
Wuhan, China
smartcjh@hust.edu.cn

Wei Jiang
School of AIA, Huazhong University
of Science and Technology
Wuhan, China
jwei0303@hust.edu.cn

Zhan Peng
School of AIA, Huazhong University
of Science and Technology
Wuhan, China
peng_zhan@hust.edu.cn

Zhiyu Pan*
School of AIA, Huazhong University
of Science and Technology
Wuhan, China
zhiyupan@hust.edu.cn

Zhiguo Cao
School of AIA, Huazhong University
of Science and Technology
Wuhan, China
zgcao@hust.edu.cn



Figure 1: Qualitative comparison between the proposed method and HDRFlow [43] on two different scenes. The input low dynamic range (LDR) videos consist of frames with alternate exposures, meaning that the exposure changes and part of exposure information is missing at every time stamp (1-st row). Prior arts, e.g., the HDRFlow, struggle to achieve temporally consistent high dynamic range (HDR) results due to the exposure change and the motion that causes information loss (2-nd row). In contrast, the proposed method achieves temporally consistent HDR reconstruction results (4-th row) by completing the absent exposure frames (3-rd row) at each time stamp. “EV”: the exposure value for each input LDR frame. “EC”: our exposure completing results for the absent exposure corresponding to the input LDR frames.

*Corresponding author.

Permission to make digital or hard copies of all or part of this work for personal or classroom use is granted without fee provided that copies are not made or distributed for profit or commercial advantage and that copies bear this notice and the full citation on the first page. Copyrights for components of this work owned by others than the author(s) must be honored. Abstracting with credit is permitted. To copy otherwise, or republish, to post on servers or to redistribute to lists, requires prior specific permission and/or a fee. Request permissions from permissions@acm.org.
MM '24, October 28-November 1, 2024, Melbourne, VIC, Australia

ABSTRACT

High dynamic range (HDR) video rendering from low dynamic range (LDR) videos where frames are of alternate exposures encounters significant challenges, due to the exposure change and absence at each time stamp. The exposure change and absence make

© 2024 Copyright held by the owner/author(s). Publication rights licensed to ACM.
ACM ISBN 979-8-4007-0686-8/24/10...\$15.00
<https://doi.org/10.1145/3664647.3680935>

existing methods generate flickering HDR results. In this paper, we propose a novel paradigm to render HDR frames via completing the absent exposure information, hence the exposure information is complete and consistent. Our approach involves interpolating neighbor LDR frames in the time dimension to reconstruct LDR frames for the absent exposures. Combining the interpolated and given LDR frames, the complete set of exposure information is available at each time stamp. This benefits the fusing process for HDR results, reducing noise and ghosting artifacts therefore improving temporal consistency. Extensive experimental evaluations on standard benchmarks demonstrate that our method achieves state-of-the-art performance, highlighting the importance of absent exposure completing in HDR video rendering. The code is available at <https://github.com/cuijiahao666/NECHDR>.

CCS CONCEPTS

• **Computing methodologies** → **Artificial intelligence; Computer vision; Image and video acquisition; Computational photography.**

KEYWORDS

HDR video, Temporal consistency, Exposure completing

ACM Reference Format:

Jiahao Cui, Wei Jiang, Zhan Peng, Zhiyu Pan, and Zhiguo Cao. 2024. Exposure Completing for Temporally Consistent Neural High Dynamic Range Video Rendering. In *Proceedings of the 32nd ACM International Conference on Multimedia (MM '24), October 28–November 1, 2024, Melbourne, VIC, Australia*. ACM, New York, NY, USA, 13 pages. <https://doi.org/10.1145/3664647.3680935>

1 INTRODUCTION

Compared with the high dynamic range (HDR) of natural scenes, the standard digital camera can only capture low dynamic range (LDR) information. To achieve the goal of “what you see is what you get” in computational photography [10, 37, 38], delicate optical systems [23, 34, 41] are designed to simultaneously capture LDR images with different exposures which cover the whole dynamic range to reconstruct HDR results. However, these systems are expensive and un-portable, making HDR contents not easily accessible for general users [19]. To address this limitation, computational methods [18, 19, 30] are designed to render HDR videos from LDR videos whose frames are exposed alternately with different exposures (as shown in 1-st row in Fig. 1).

In this setting, the incomplete exposure information varies along the time dimension. Existing neural HDR rendering methods [3, 6, 16, 43] align neighbor LDR frames according to the LDR frame of current time stamp (called reference frame in this paper) and fuse the aligned neighbor LDR frames into the reference frame to supplement the missing exposure information. The exposure of reference frame changes at every time stamp, which means that the reference frames of different exposures may have different defects: saturation for highly exposed LDR frames, and noise for lowly exposed ones. Due to that the methods mentioned above heavily depend on reference frames, HDR results from these methods may inherit defects of the reference frames, suffering from the artifacts, *i.e.*, the ghosting (2-nd row in Fig. 1(a)) and noise (2-nd row in Fig. 1(b)), thereby causing temporal inconsistency.

To tackle this problem, we revisit early traditional methods [18, 19] for HDR rendering and are motivated to complete the missing exposure information for each time stamp [18, 19]. This idea follows the philosophy of optical HDR systems [41] that are designed to obtain different exposed LDR frames at exact the same time. In this way, defects of different exposed frames can be mutually compensated. In this paper, we propose the Neural Exposure Completing HDR (NECHDR) framework to reconstruct the LDR frames with missing exposure information. In this way, full exposure information at each time stamp can be covered by the reference and completed LDR frames, therefore the exposure information is complete and consistent along the time dimension, which benefits the temporal consistency of the rendered HDR videos.

In the proposed NECHDR framework, pyramid features of input LDR frames are extracted by the feature encoder, then fed into the exposure completing decoder and the HDR rendering decoder. The exposure completing decoder interpolates the features of neighbor LDR frames at every level of the feature pyramid. The interpolated LDR features are combined with the features from input LDR images as the inputs to HDR rendering decoder. The HDR rendering decoder estimates coarse HDR results and the optical flows at every level. The flows can facilitate feature interpolating in exposure completing decoder. At the end of NECHDR, a simple blending network is used to integrate interpolated LDR frames, input frames, and coarse HDR frames, which can achieve high-quality and temporally consistent HDR reconstruction results.

Extensive experimental results on multiple public benchmarks demonstrate the superiority of the proposed NECHDR: by completing the missing exposure information (3-rd row in Fig. 1), our method mitigates ghosting resulting from large motions for the time stamps with highly exposed reference frames (4-th row in Fig. 1(a)), and reduces the noise level for the lowly exposed reference frames (4-th row in Fig. 1(b)), hence achieves better temporal consistency. Our work sheds light again on the exposure completing for HDR video rendering. The contributions can be summarized as follows:

- Our work firstly implements the idea of exposure completing for neural HDR rendering.
- Our work proposes a novel HDR video rendering framework, *a.k.a.*, the NECHDR, which completes the missing exposure information by interpolating LDR frames.
- Our NECHDR achieves new state-of-the-art performance on current benchmarks.

2 RELATED WORK

2.1 HDR Image Rendering

HDR imaging technology aims to extend the dynamic range of images by merging LDR images with different exposures. Both the HDR image and video reconstructing tasks encounter the misalignment between LDR images. Pioneer studies for HDR image rendering employ image alignment techniques to address this issue. Early works [9, 13, 20, 25, 36, 50] often align LDR images globally, then detect and discard unaligned regions.

Directly discarding these regions leads to significant information loss, posing challenges for HDR image rendering. To address these issues, optical-flow-based [1, 15, 52] and patch-based methods [14, 29, 40] are proposed. However, large motion still makes

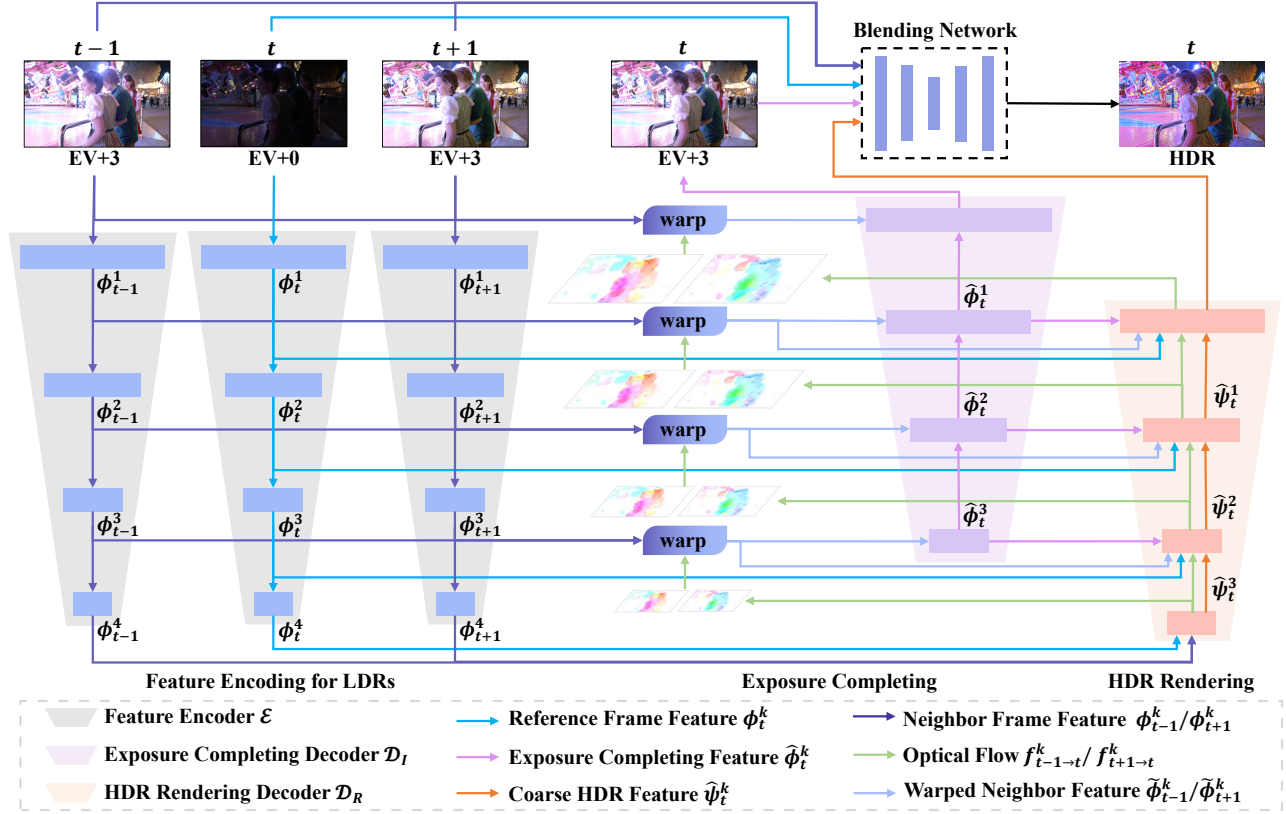


Figure 2: Pipeline of the proposed NECHDR network. Our network mainly consists of three processes: feature encoding for LDRs, exposure completing for LDR frames with missing exposures, and HDR rendering. We extract pyramid features from the input LDR frames using a parameter shared feature encoder. Then, the optical flows predicted by the lower-level HDR rendering decoder is used to warp neighbor frames to the reference frame. Subsequently, the exposure completing decoder performs exposure completing based on the warped neighbor frame features. The input features and the completed feature are fed into the HDR rendering decoder to render the coarse HDR frame. Finally, the original frames, the completed frame, and the coarse HDR frame are fused together through a simple blending network to produce a high-quality HDR result.

these methods fail to produce artifact-free HDR results. With the rapid development of deep learning, many studies for HDR image rendering switch their focus to neural networks [2, 5, 17, 26, 28, 35, 42, 45–47], achieving promising results. Kalantari *et al.* [17] propose using neural networks to align input LDR images with predicted optical flow. Wu *et al.* [42] directly map LDR images to HDR images, thereby avoiding alignment errors. Yan *et al.* [46, 48] use spatial attention to implicitly align LDR images, achieving further improvement. Liu [28] *et al.* introduce a ghost-free imaging model based on swin-transformer [27]. Yan *et al.* [45] utilize patch-based and pixel-based fusion to search for information to complement the reference frame from the other frames. However, these HDR image rendering methods assume a fixed exposure for reference frames, typically medium exposure, therefore is not suitable for HDR video rendering where reference frames have alternating exposures.

2.2 HDR Video Rendering

HDR video can be obtained by delicate optical systems, such as scan-line exposure/ISO [4, 12], internal/external beam splitter [24, 32, 41],

modulo camera [51] and neuromorphic camera [11]. However, these expensive systems are hardly accessible to general users. Therefore, rendering HDR videos from LDR videos is investigated. Kang *et al.* [19] utilize both global and local alignment for reference frames with neighbor frames. Kalantari *et al.* [18] propose a patch-based optimization algorithm to reconstruct HDR video by synthesizing missing exposures for each frame. These traditional methods offer a fundamental idea for completing missing exposures, but they require iterative optimization and are prone to producing artifacts. Recently, Kalantari *et al.* [16] introduce an end-to-end neural network consisting of an optical flow prediction model and a fusion network. Chen *et al.* [3] propose a coarse-to-fine alignment framework, which utilizes optical flow for coarse alignment and then employs deformable convolution [7] for fine alignment. Chung *et al.* [6] employ spatial attention instead of optical flow to achieve alignment from adjacent frames to the reference frame. Xu *et al.* [43] propose the HDR-domain loss, which uses optical flow supervised by HDR frames for LDR alignment, yielding favorable results. However, when complex situations such as large motion, saturation,

and others occur simultaneously, these methods struggle to achieve precise alignment, resulting in artifacts in the final outputs. Besides, as the exposures of reference frames alternate, the reconstructed HDR frames tend to inherit the defects of reference frames, leading to flicker in the output videos. The fundamental issue lies in the lack of exposure information at every time stamp. Different from previous methods, we propose a renaissance work which focuses on completing missing exposures for the reference frame in neural HDR video rendering. Through compensating for the defects of the alternatively exposed reference frames by utilizing the completed results, our approach avoids artifacts of ghost and noise and obtains a temporally consistent HDR video result.

3 PROPOSED METHODS

3.1 Overview

Each frame l_i in the LDR video $L = \{l_i | i = 1, \dots, n\}$ is expected to have multiple exposures $E = \{\epsilon_i | i = 1, \dots, z\}$ to cover the whole dynamic range of HDR video $H = \{h_i | i = 1, \dots, n\}$, where n is the length of video, and z is the number of exposures. However, in our task, only one exposure can be obtained in one certain time stamp, which creates an exposure sequence $E = \{\epsilon_i | i = 1, \dots, n\}$ for the LDR video, where $\epsilon_i = \epsilon_{(i \oslash z) + 1}$. $a \oslash b$ indicates the remainder of a divided by b .

Following previous work [43], we try to render a high-quality HDR video with LDR video under two settings of different alternate exposures: two alternate exposures ($z = 2$) with three frames as input, and three alternate exposures ($z = 3$) with five frames. We use the two-exposure setting as an example to demonstrate how to achieve HDR rendering. In Sec. 3.5, we introduce how to extend our approach to the three-exposure setting. The frame l_t corresponding to the current time stamp t , is treated as the reference frame. l_t is combined with its neighbors as input $\{l_{t-1}, l_t, l_{t+1}\}$. To render HDR frames, we explicitly complete frames \tilde{l}_t with absent exposure ϵ_i , where $i \neq (t \oslash z) + 1$. Therefore, with complete exposure information, we can render a high-quality HDR video.

Our method consists of two processes: exposure completing for the frame with the absent exposure at the time stamp t and coarse-to-fine HDR rendering. These two processes are coupled together through an encoder-decoder architecture, as illustrated in the Fig. 2. The feature encoder \mathcal{E} takes LDR frames $\{l_{t-1}, l_t, l_{t+1}\}$ as input and generates pyramid features for each frame. As the spatial dimensions decrease and the feature channels increase, the encoder outputs feature sets $\{\Phi_{t-1}, \Phi_t, \Phi_{t+1}\}$ for input frames, each of which is a set of k -level pyramid features $\Phi = \{\phi^k | k = 1, 2, 3, 4\}$. Considering the distinct characteristics of the two processes, we devise two dedicated decoders. Initially, an exposure completing decoder \mathcal{D}_I is employed to interpolate frame \tilde{l}_t and its corresponding features $\tilde{\Phi}_t^k = \{\tilde{\phi}_t^k | k = 1, 2, 3\}$. Subsequently, a coarse-to-fine HDR rendering decoder \mathcal{D}_R takes $\{\Phi_{t-1}, \Phi_t, \Phi_{t+1}\}$ and $\tilde{\Phi}_t$ as input, and outputs optical flows $F_{t-1 \rightarrow t} = \{f_{t-1 \rightarrow t}^k | k = 0, 1, 2, 3\}$, $F_{t+1 \rightarrow t} = \{f_{t+1 \rightarrow t}^k | k = 0, 1, 2, 3\}$, coarse HDR features $\tilde{\Psi}_t = \{\tilde{\psi}_t^k | k = 1, 2, 3\}$ and coarse HDR frame \tilde{h}_t^c . The optical flows here are utilized to warp $\{\Phi_{t-1}, \Phi_{t+1}\}$ or $\{l_{t-1}, l_{t+1}\}$ to time stamp t , yielding warped neighbor features $\tilde{\Phi}_{t-1} = \{\tilde{\phi}_{t-1}^k | k = 1, 2, 3\}$, $\tilde{\Phi}_{t+1} = \{\tilde{\phi}_{t+1}^k | k = 1, 2, 3\}$ or frames $\{\tilde{l}_{t-1}, \tilde{l}_{t+1}\}$. The warped neighbor features $\{\tilde{\Phi}_{t-1}, \tilde{\Phi}_{t+1}\}$

and frames $\{\tilde{l}_{t-1}, \tilde{l}_{t+1}\}$ are fed into \mathcal{D}_I . Subsequently, the exposure completing features $\tilde{\Phi}_t$ from \mathcal{D}_I are fed into the HDR rendering decoder \mathcal{D}_R , assisting it in better restoring lost details due to saturation and noise when decoding coarse HDR features $\tilde{\Psi}_t$ and coarse HDR frame \tilde{h}_t^c . This design coupling two decoders enables mutual enhancement of the two processes, thus obtaining more accurate exposure completing frame \tilde{l}_t and better coarse HDR result \tilde{h}_t^c . To obtain the final HDR rendering result, we map $\{l_{t-1}, l_t, l_{t+1}\}$ and \tilde{l}_t to the linear HDR domain. The function defining the mapping of LDR frames to the linear HDR domain is as follows:

$$x_t = l_t^\gamma / e_t, \quad (1)$$

where γ is a hyperparameter and e_t is the exposure time of l_t . Finally, the ultimate high-quality HDR rendering result \hat{h}_t is obtained by fusing the input and completed frames with coarse HDR frame in linear HDR domain using a simple blending network. The details of each process will be presented in the following sections.

3.2 Exposure Completing

Under the setting that input LDR frames are with alternating exposures, completing the absent exposure information is essential for rendering HDR frames. However, existing neural HDR rendering methods overlook this essential problem, making it difficult for these methods to accurately recover detailed information when motion occurs with saturation or noise simultaneously, potentially leading to artifacts. Furthermore, due to these methods heavily depend on reference frames, the alternate appearance of noise and saturation caused by the alternate exposures in reference frames affects the temporal consistency of the video. Therefore, to better address the aforementioned issues, we explicitly tackle the fundamental problem of HDR rendering by completing frames with absent exposure corresponding to reference frames.

Given the LDR frame input $\{l_{t-1}, l_t, l_{t+1}\}$ with alternate exposures $\{\epsilon_{t-1}, \epsilon_t, \epsilon_{t+1}\}$, where the reference frame and neighbor frames have two different exposures ($\epsilon_t = \epsilon_1$ and $\epsilon_{t-1} = \epsilon_{t+1} = \epsilon_2$), our task is to complete the frame \tilde{l}_t with absent exposure ϵ_2 corresponding to reference frame through interpolation.

Our exposure completing process takes the neighbor features $\{\Phi_{t-1}, \Phi_{t+1}\}$ and the optical flows $\{F_{t-1 \rightarrow t}, F_{t+1 \rightarrow t}\}$ as input. During this process, for the features with absent exposure information, the k -th level neighbor features $\{\phi_{t-1}^k, \phi_{t+1}^k\}$ and optical flows $\{f_{t-1 \rightarrow t}^k, f_{t+1 \rightarrow t}^k\}$ are processed to obtain completed feature $\tilde{\phi}_t^k$:

$$\tilde{\phi}_{t-1}^k, \tilde{\phi}_{t+1}^k = \mathcal{W}(\phi_{t-1}^k, f_{t-1 \rightarrow t}^k), \mathcal{W}(\phi_{t+1}^k, f_{t+1 \rightarrow t}^k), \quad (2)$$

$$\tilde{\phi}_t^3 = \mathcal{D}_I^3 \left(\left[\tilde{\phi}_{t-1}^3, \tilde{\phi}_{t+1}^3 \right] \right), \quad (3)$$

$$\tilde{\phi}_t^k = \mathcal{D}_I^k \left(\left[\tilde{\phi}_{t-1}^k, \tilde{\phi}_{t+1}^k, \mathcal{U}_2(\tilde{\phi}_t^{k+1}) \right] \right), \quad (4)$$

where $\mathcal{W}(\cdot, \cdot)$ denotes using optical flow to warp neighbor features to the reference feature, \mathcal{U}_2 represents the bilinear upsampling operation with scale factor 2, \mathcal{D}_I^k ($k = 1, 2$) represents the middle levels of the exposure completing decoder \mathcal{D}_I , and $[\cdot]$ indicates concatenation operation. In the final step of the exposure completing process, the completed frame \tilde{l}_t is explicitly interpolated with

neighbor frames l_{t-1}, l_{t+1} and optical flow $f_{t-1 \rightarrow t}^0, f_{t+1 \rightarrow t}^0$ as input:

$$\tilde{l}_{t-1}, \tilde{l}_{t+1} = \mathcal{W}(l_{t-1}, f_{t-1 \rightarrow t}^0), \mathcal{W}(l_{t+1}, f_{t+1 \rightarrow t}^0), \quad (5)$$

$$\hat{l}_t = \mathcal{D}_I^0 \left(\left[\tilde{l}_{t-1}, \tilde{l}_{t+1}, \mathcal{U}_2(\hat{\phi}_t^1) \right] \right), \quad (6)$$

where \mathcal{D}_I^0 represents the highest level of the exposure completing decoder \mathcal{D}_I .

As illustrated in the Fig. 1, with the above design, we have obtained realistic exposure completing result for the challenging areas with motion, saturation and noise, providing accurate and complete exposure information for subsequent HDR rendering.

3.3 Coarse-to-fine HDR Rendering

Building upon the results of above process, we designed a coarse-to-fine HDR rendering network based on completed features $\hat{\Phi}_t$ and frame \hat{l}_t . Taking the original features $\{\Phi_{t-1}, \Phi_t, \Phi_{t+1}\}$, completed features $\hat{\Phi}_t$ and warped neighbor features $\{\hat{\Phi}_{t-1}, \hat{\Phi}_{t+1}\}$ as input, the HDR rendering decoder \mathcal{D}_R reconstructs HDR features $\hat{\Psi}_t$ and optical flows $\{F_{t-1 \rightarrow t}, F_{t+1 \rightarrow t}\}$ in a coarse-to-fine manner, and finally obtains the coarse HDR frame \hat{h}_t^c :

$$\hat{\psi}_t^3, f_{t-1 \rightarrow t}^3, f_{t+1 \rightarrow t}^3 = \mathcal{D}_R^4 \left(\left[\phi_{t-1}^4, \phi_t^4, \phi_{t+1}^4 \right] \right), \quad (7)$$

$$\begin{aligned} & \hat{\psi}_t^{k-1}, f_{t-1 \rightarrow t}^{k-1}, f_{t+1 \rightarrow t}^{k-1} = \\ & \mathcal{D}^k \left(\left[\phi_t^k, \hat{\phi}_t^k, \hat{\psi}_t^k, f_{t-1 \rightarrow t}^k, f_{t+1 \rightarrow t}^k, \hat{\phi}_{t-1}^k, \hat{\phi}_{t+1}^k \right] \right), \end{aligned} \quad (8)$$

$$\begin{aligned} & \hat{h}_t^c, f_{t-1 \rightarrow t}^0, f_{t+1 \rightarrow t}^0 = \\ & \mathcal{D}^1 \left(\left[\phi_t^1, \hat{\phi}_t^1, \hat{\psi}_t^1, f_{t-1 \rightarrow t}^1, f_{t+1 \rightarrow t}^1, \hat{\phi}_{t-1}^1, \hat{\phi}_{t+1}^1 \right] \right), \end{aligned} \quad (9)$$

where \mathcal{D}_R^k ($k = 2, 3$) stand for the k -th level of the HDR rendering decoder \mathcal{D}_R . The warped neighbor features $\{\hat{\phi}_{t-1}^k, \hat{\phi}_{t+1}^k\}$ help \mathcal{D}_R to identify regions with poor alignment and subsequently obtain the refined optical flow $\{f_{t-1 \rightarrow t}^{k-1}, f_{t+1 \rightarrow t}^{k-1}\}$.

Based on the completed frame \hat{l}_t and the coarse HDR frame \hat{h}_t^c , we combine them with original LDR frames to obtain the final HDR rendering result \hat{h}_t . We adopted a blending network with U-net architecture from Xu *et al.* [43]. Thus, original and completed LDR frames $\{l_{t-1}, l_t, l_{t+1}, \hat{l}_t\}$, along with their corresponding frames $\{x_{t-1}, x_t, x_{t+1}, \hat{x}_t\}$ in linear HDR domain, and coarse HDR frame \hat{h}_t^c are fed into the blending network. The blending network calculates fusion weights $W = \{w_i | i = 0, 1, 2, 3, 4\}$ for the input five HDR domain frames $\{x_{t-1}, x_t, x_{t+1}, \hat{x}_t, \hat{h}_t^c\}$ and obtains the final HDR rendering result \hat{h}_t through a weighted average based on the computed weights W :

$$\hat{h}_t = \frac{w_0 \hat{h}_t^c + w_1 \hat{x}_t + w_2 x_t + w_3 x_{t-1} + w_4 x_{t+1}}{\sum_{j=0}^4 w_j}. \quad (10)$$

Following Xu *et al.* [43], we also fuse with the neighbor frames $\{x_{t-1}, x_{t+1}\}$ to provide information about static regions. As depicted in Fig. 1, when encountering complex scenes involving both motion and saturation or noise, the fused exposure completion frames effectively provide the missing exposure information, thereby obtaining ghost-free and low-noise HDR results. In summary, based on completing the frame with missing exposure information, we finally achieve a high-quality HDR rendering process.

3.4 Training Loss

We calculate the losses for the completed LDR features $\hat{\Phi}_t$ and frame \hat{l}_t , rendered HDR features $\hat{\Psi}_t$ and frame \hat{h}_t , and optical flows $\{F_{t-1 \rightarrow t}, F_{t+1 \rightarrow t}\}$:

The losses for images. The widely adopted \mathcal{L}_1 loss is used to supervise the completed LDR frame \hat{l}_t and rendered HDR frame \hat{h}_t , and is defined as follows:

$$\mathcal{L}_I^{com} = \left\| \hat{l}_t - \bar{l}_t \right\|_1, \quad (11)$$

$$\mathcal{L}_I^{ren} = \left\| \mathcal{T}(\hat{h}_t) - \mathcal{T}(\bar{h}_t) \right\|_1, \quad (12)$$

$$\mathcal{L}_I = \mathcal{L}_I^{com} + \mathcal{L}_I^{ren}, \quad (13)$$

where \bar{l}_t and \bar{h}_t are the corresponding ground truth for the completed LDR frame \hat{l}_t and rendered HDR frame \hat{h}_t , respectively. The $\mathcal{T}(\cdot)$ is a widely used function to map HDR frame to the tone-mapped HDR domain, since HDR images are typically displayed after tone mapping. This simple differentiable μ -law function $\mathcal{T}(\cdot)$ is defined as follows:

$$\mathcal{T}(h) = \frac{\log(1 + \mu h)}{\log(1 + h)}, \quad (14)$$

where μ is a hyperparameter.

The losses for features. Feature space geometry loss proposed in [22] is employed to ensure that the intermediate features obtained from frame interpolation and HDR reconstruction can be more effectively refined to conform to geometrically structured features. The parameter shared encoder \mathcal{E} is used to obtain corresponding pyramid features $\bar{\Phi}_t = \{\bar{\phi}_t^k | k = 1, 2, 3\}$ and $\bar{\Psi}_t = \{\bar{\psi}_t^k | k = 1, 2, 3\}$ from the ground truth of completed LDR and rendered HDR frames. Then, the loss function for supervising the features of completed LDR and rendered HDR frames can be written as:

$$\mathcal{L}_G^{com} = \sum_{k=1}^3 \mathcal{L}_{cen}(\bar{\phi}_t^k, \hat{\phi}_t^k), \quad (15)$$

$$\mathcal{L}_G^{ren} = \sum_{k=1}^3 \mathcal{L}_{cen}(\bar{\psi}_t^k, \hat{\psi}_t^k), \quad (16)$$

$$\mathcal{L}_G = \mathcal{L}_G^{com} + \mathcal{L}_G^{ren}, \quad (17)$$

where the \mathcal{L}_{cen} is census loss [33] and computed using the soft Hamming distance between census-transformed [49] feature maps, considering 3×3 patches in a channel-by-channel manner.

The loss for optical flows. The HDR-domain alignment loss [43] is used hierarchically to supervise the learning process of optical flow, which is defined as follows:

$$\mathcal{L}_F^{t-1 \rightarrow t} = \sum_{k=0}^3 \left\| \mathcal{W}(\mathcal{T}(\bar{h}_{t-1}), \mathcal{U}_{2^k}(f_{t-1 \rightarrow t}^k)) - \mathcal{T}(\bar{h}_t) \right\|_1, \quad (18)$$

$$\mathcal{L}_F^{t+1 \rightarrow t} = \sum_{k=0}^3 \left\| \mathcal{W}(\mathcal{T}(\bar{h}_{t+1}), \mathcal{U}_{2^k}(f_{t+1 \rightarrow t}^k)) - \mathcal{T}(\bar{h}_t) \right\|_1, \quad (19)$$

$$\mathcal{L}_F = (1 - m_t) \odot (\mathcal{L}_F^{t-1 \rightarrow t} + \mathcal{L}_F^{t+1 \rightarrow t}), \quad (20)$$

where $\mathcal{W}(\cdot, \cdot)$ denotes using optical flow to warp neighbor frames to the reference frame, \mathcal{U}_s represents the bilinear upsampling operation with scale factor s . The mask m_t indicates well-exposed regions in reference frame. First, l_t is converted to YCbCr color space to

Table 1: Quantitative comparisons of our method with other state-of-the-art methods on the Cinematic Video dataset [8]. The best and the second best results are highlighted in red and blue, respectively.

Methods		2-Exposure			3-Exposure		
		PSNR _T	SSIM _T	HDR-VDP-2	PSNR _T	SSIM _T	HDR-VDP-2
Kalantari13 [18]	2013-TOG	37.51	0.9016	60.16	30.36	0.8133	57.68
Kalantari19 [16]	2019-CGF	37.06	0.9053	70.82	33.21	0.8402	62.44
Yan19 [46]	2019-CVPR	31.65	0.8757	69.05	34.22	0.8604	66.18
Prabhakar [39]	2021-CVPR	34.72	0.8761	68.82	34.02	0.8633	65.00
Chen [3]	2021-ICCV	35.65	0.8949	72.09	34.15	0.8847	66.81
LAN-HDR [6]	2023-ICCV	38.22	0.9100	69.15	35.07	0.8695	65.42
HDRFlow [43]	2024-CVPR	39.20	0.9154	70.98	36.55	0.9039	65.89
HDRFlow [43](+Sintel)	2024-CVPR	39.30	0.9156	71.05	36.65	0.9055	66.02
Ours	2024-MM	40.59	0.9241	73.31	37.24	0.9102	68.36

Table 2: Quantitative comparisons of our method with other state-of-the-art methods on the DeepHDRVideo dataset [3]. The result is the weighted average of all results from both dynamic scenes and static scenes in this dataset. The best and the second best results are highlighted in red and blue, respectively.

Methods		2-Exposure			3-Exposure		
		PSNR _T	SSIM _T	HDR-VDP-2	PSNR _T	SSIM _T	HDR-VDP-2
Kalantari13 [18]	2013-TOG	40.33	0.9409	66.11	38.45	0.9489	57.31
Kalantari19 [16]	2019-CGF	39.91	0.9329	71.11	38.78	0.9331	65.73
Yan19 [46]	2019-CVPR	40.54	0.9452	69.67	40.20	0.9531	68.23
Prabhakar [39]	2021-CVPR	40.21	0.9414	70.27	39.48	0.9453	65.93
Chen [3]	2021-ICCV	42.48	0.9620	74.80	39.44	0.9569	67.76
LAN-HDR [6]	2023-ICCV	41.59	0.9472	71.34	40.48	0.9504	68.61
HDRFlow [43]	2024-CVPR	43.18	0.9510	77.11	40.45	0.9530	72.30
HDRFlow [43](+Sintel)	2024-CVPR	43.25	0.9520	77.29	40.56	0.9535	72.42
Ours	2024-MM	43.44	0.9558	79.20	40.13	0.9550	76.98

extract luminance y . Then, m_t is defined as $\delta_{\text{low}} < y < \delta_{\text{high}}$, where δ_{low} and δ_{high} are the low and high luminance thresholds, respectively. This allows the optical flow computation to focus more on regions with poor exposure in the reference frame.

Total loss. Our total loss can be summarized as follows:

$$\mathcal{L}_{\text{total}} = \mathcal{L}_I + \alpha * \mathcal{L}_G + \beta * \mathcal{L}_F. \quad (21)$$

3.5 Extension to Three Exposures

In the alternate exposure setting with three exposures, five LDR frames $\{l_{t-2}, l_{t-1}, l_t, l_{t+1}, l_{t+2}\}$ are used as input to the network for HDR \hat{h}_t rendering. The five LDR frames are with corresponding exposure sequences $\{e_{t-2}, e_{t-1}, e_t, e_{t+1}, e_{t+2}\}$. In this way, the reference frame has only one certain exposure $e_t = \epsilon_3$. Specifically, the first frame l_{t-2} and the fourth frame l_{t+1} have the same exposure $e_{t-2} = e_{t+1} = \epsilon_1$, while the second frame l_{t-1} and the fifth frame l_{t+2} also share the same exposure $e_{t-1} = e_{t+2} = \epsilon_2$. Therefore, the exposure completion process takes $\{l_{t-2}, l_t, l_{t+1}\}$ and $\{l_{t-1}, l_t, l_{t+2}\}$ as inputs, generates exposure completing results $\{\hat{l}_t^{\epsilon_1}, \hat{l}_t^{\epsilon_2}\}$ through the flow-guided completing process, and obtains coarse HDR results \hat{h}_t^c through the coarse-to-fine HDR rendering process. A total of fifteen images, including the exposure completing frames and multiple original LDR frames, along with their corresponding frames

in linear HDR domain, and the coarse HDR result, are fed into the blending network. This blending network calculates seven weights to fuse the seven HDR domain images in a weighted average manner and obtain the final HDR rendering result.

4 EXPERIMENTS

4.1 Experimental Setup

Datasets. We utilize synthetic training data generated from the Vimeo-90K dataset [44]. To adapt the Vimeo90K dataset for HDR video reconstruction, we follow prior research [19] to convert the original data into LDR sequences with alternate exposures. To create the ground truth of completed LDR frames, we also generated LDR sequences with missing exposures in the same way. Our framework is tested on the Cinematic Video dataset [8] and DeepHDRVideo dataset [3]. The Cinematic Video dataset has two synthetic videos from indoor and outdoor scenes. The DeepHDRVideo dataset [3] contains both real-world dynamic scenes and static scenes with random global motion augmentation. The HDRVideo dataset [18] is employed solely for qualitative evaluation, as it lacks ground truth. **Implementation details.** We implement our approach using PyTorch and conduct experiments on an NVIDIA RTX3090 GPU. We employ AdamW optimizer [21] with $\beta_1 = 0.9$ and $\beta_2 = 0.999$. The learning rate is set to 10^{-4} . In our experiments, we set γ in Eq. 1 to

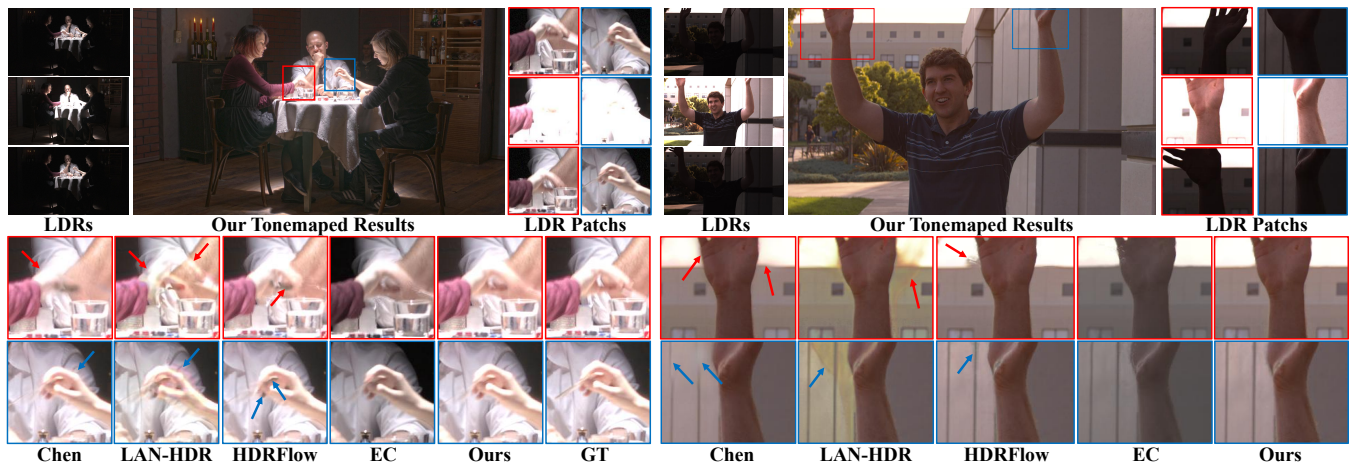


Figure 3: Qualitative comparison in scenes with over-saturation and motion. Left: 2-Exposure scene from the Cinematic Video dataset [8]. Right: 2-Exposure scene from the HDRVideo dataset [18]. "EC" refers to our exposure completion results.

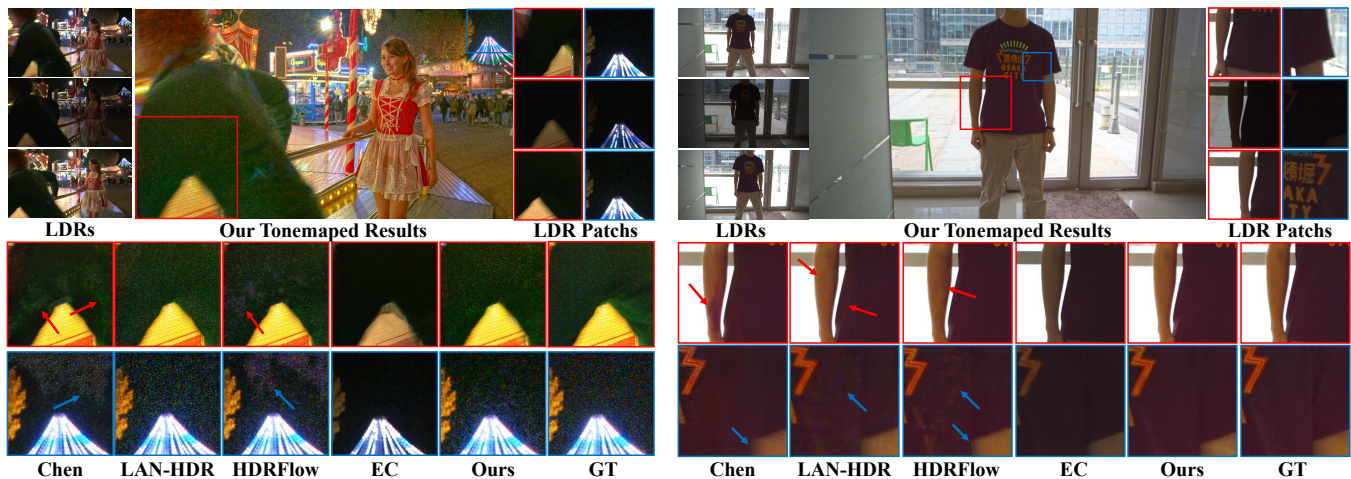


Figure 4: Qualitative comparison in scenes with noise and motion. Left: 2-Exposure scene from the Cinematic Video dataset [8]. Right: 2-Exposure scene from the DeepHDRVide dataset [3]. "EC" refers to our exposure completion results.

2.2 and μ in Eq. 14 to 5000. Following HDRFlow [43], we set δ_{low} to 0.2 and δ_{high} to 0.8. The weighting hyperparameters α and β for the loss function in Eq. 21 are set to 0.01.

Evaluation metrics. PSNR_T, SSIM_T and HDR-VDP-2 [31] are adopted as the evaluation metrics. PSNR_T and SSIM_T are computed on the tone-mapped images. HDR-VDP-2 is computed with the number of pixels per visual degree set to 30, which means the angular resolution of the image.

4.2 Comparisons with State-of-the-art

Quantitative comparisons between our and other state-of-the-art methods on the Cinematic Video [8] and DeepHDRVide [3] datasets are shown in Table 7 and Table 2, respectively. Compared to state-of-the-art methods, our approach consistently achieves superior or comparable performance. Especially, our approach achieves state-of-the-art performance on Cinematic Video [8] dataset, outperforming the second-best method by 1.29dB and 0.59dB in terms of PSNR_T for the 2-exposure and 3-exposure settings, respectively.

Qualitative comparisons are shown in Fig. 3 and Fig. 4. we compare our NECHDR with the previous methods: Chen [3], LAN-HDR [6] and HDRFlow [43]. Fig. 3 illustrates the results from scenes with saturation and motion on Cinematic Video dataset [8] and HDRVideo dataset [18] under the 2-exposure setting. Apart from our method, other methods tend to exhibit severe artifacts or detail loss when saturation and motion occur simultaneously. In such challenging scenarios, we achieve accurate and artifact-free exposure completion results for saturated regions by leveraging frame interpolation from neighboring frames. This enables us to fuse high-quality HDR results. And in Fig. 4, we also show the results encountering noise and motion from the Cinematic Video dataset [8] and DeepHDRVide dataset [3]. The scene on the left side of Fig. 4 is captured in low-light conditions, resulting in very low signal-to-noise ratio in the low-exposure frames. This can lead to very high noise levels in rendered HDR frames after tone mapping, which makes this scene particularly challenging. Specifically,

Table 3: Ablation study of NECHDR on the DeepHDRVideo [3] and CinematicVideo dataset [8]. "EC" refers to exposure completing, "HR" refers to HDR rendering. "Uncoupled" means this two processes work independently.

Model	DeepHDRVideo		Cinematic Video	
	PSNR _T	SSIM _T	PSNR _T	SSIM _T
EC Baseline	41.09	0.9479	39.13	0.9174
HR Baseline	42.64	0.9524	39.98	0.9193
Uncoupled EC, HR	43.17	0.9535	40.27	0.9202
Coupled EC, HR (Ours)	43.44	0.9558	40.59	0.9241

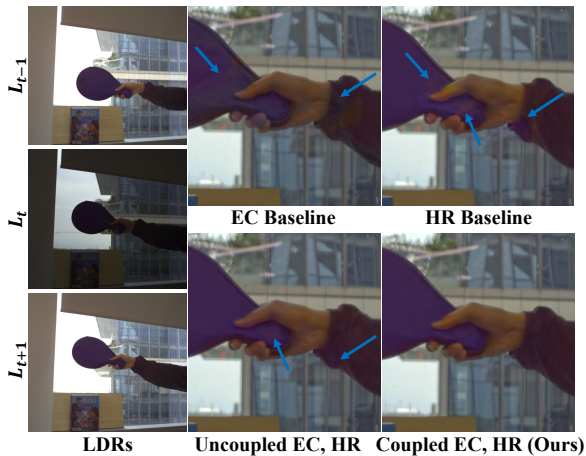


Figure 5: Qualitative comparison of the models corresponding to the ablation study on a dynamic scene of DeepHDRVideo [3] dataset.

methods based on optical flow [3, 43] tend to produce noisy artifacts, while attention-based method [6] exhibit more pronounced noise. Our method explicitly reconstructs the absent high-exposure frame with low noise at the current time stamp, achieving the best noise suppression, even with some regions having noise intensity lower than ground truth. The visualization results above explain why we achieve a significant performance improvement compared with other state-of-the-art methods.

4.3 Analysis

Ablation Study. We conduct ablation experiments under the 2-exposure setting on Cinematic Video dataset [8] and DeepHDRVideo dataset [3], and the quantitative and qualitative results are shown in Table 3 and Fig. 5, respectively. We devised a baseline that employs IFRNet [22] to utilize the neighbor frames to complete the middle time frame that with missing exposure information and achieve HDR results by simply fusing the completed LDR frame with the original LDR frames. The performance of this baseline is shown as "EC Baseline" in the first row in Table 3. Another baseline directly renders HDR results based on IFRNet, which is the "HR Baseline" in second row in Table 3. However, relying solely on either exposure completing or HDR rendering results is with limited performance. By adding the exposure completing decoder,

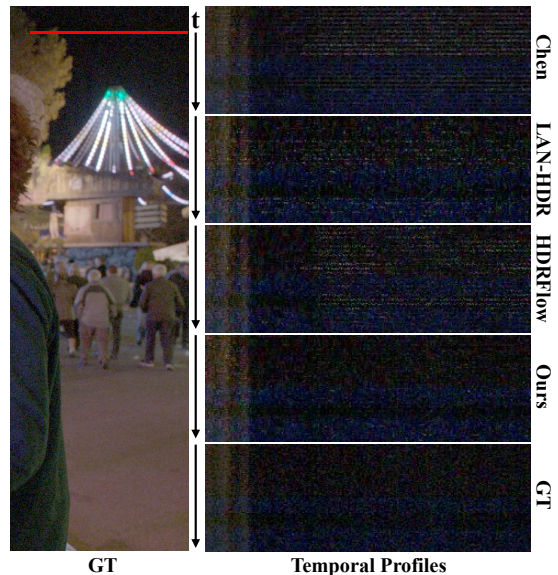


Figure 6: Visual comparisons of temporal consistency.

we get a network (third row in Table 3) that contains both decoupled exposure completing and HDR rendering processes. Finally, through feeding the completed features and frames from exposure completing decoder into the process of HDR rendering, we achieve our NECHDR framework in the fourth row in Table 3. Based on the qualitative and quantitative results, we can see: (a) coupled exposure completing and HDR rendering processes benefit the quality of final HDR results; (b) exposure completing decoder is necessary; (d) the completed results with missing exposure information help the rendering process of HDR reconstruction.

Temporal consistency. We show the visual comparisons of temporal consistency in Fig. 6. In Fig. 6, we record a two-pixel-height line traversing all frames of a scene in the Cinematic Video dataset [8] over time and lay them out sequentially to form temporal profiles. Base on the illustration of temporal profiles, we can observe that the horizontal stripes exist in the temporal profiles of other methods. The horizontal stripes comes from the differences between adjacent frames, which represents the temporal inconsistency. In contrast, the horizontal stripes can hardly be observed in our temporal profiles, which means that our proposed method achieves better temporal consistency.

5 CONCLUSION

In this paper, we implement the idea of exposure completing for neural HDR video rendering and propose the Neural Exposure Completing HDR (NECHDR) framework. The NECHDR leverages interpolation of neighbor LDR frames to complete missing exposures, providing a complete set of exposure information for each time stamp. This process of exposure completing creates a novel neural HDR video rendering pipeline, which can generate results of less noise and ghosting artifacts, thereby enhancing temporal consistency. Experimental results on multiple public benchmarks demonstrate the superiority of our NECHDR, which may shift the focus of researchers in this area to the exposure completing.

REFERENCES

- [1] Luca Bogoni. 2000. Extending dynamic range of monochrome and color images through fusion. In *Int. Conf. Pattern Recog.*, Vol. 3. IEEE, 7–12.
- [2] Sibi Catley-Chandar, Thomas Tanay, Lucas Vandroux, Aleš Leonardis, Gregory Slabaugh, and Eduardo Pérez-Pellitero. 2022. Flexhdr: Modeling alignment and exposure uncertainties for flexible hdr imaging. *IEEE Trans. Image Process.* 31 (2022), 5923–5935.
- [3] Guanying Chen, Chaofeng Chen, Shi Guo, Zhetong Liang, Kwan-Yee K Wong, and Lei Zhang. 2021. HDR video reconstruction: A coarse-to-fine network and a real-world benchmark dataset. In *Proc. Int. Conf. Comput. Vis.* 2502–2511.
- [4] Inchang Choi, Seung-Hwan Baek, and Min H Kim. 2017. Reconstructing interlaced high-dynamic-range video using joint learning. *IEEE Trans. Image Process.* 26, 11 (2017), 5353–5366.
- [5] Haesoo Chung and Nam Ik Cho. 2022. High dynamic range imaging of dynamic scenes with saturation compensation but without explicit motion compensation. In *Proc. IEEE Winter Conf. Appl. Comput. Vis.* 2951–2961.
- [6] Haesoo Chung and Nam Ik Cho. 2023. LAN-HDR: Luminance-based Alignment Network for High Dynamic Range Video Reconstruction. In *Proc. Int. Conf. Comput. Vis.* 12760–12769.
- [7] Jifeng Dai, Haozhi Qi, Yuwen Xiong, Yi Li, Guodong Zhang, Han Hu, and Yichen Wei. 2017. Deformable convolutional networks. In *Proc. Int. Conf. Comput. Vis.* 764–773.
- [8] Jan Froehlich, Stefan Grandinetti, Bernd Eberhardt, Simon Walter, Andreas Schilling, and Harald Brendel. 2014. Creating cinematic wide gamut HDR-video for the evaluation of tone mapping operators and HDR-displays. In *Digital photography X*, Vol. 9023. SPIE, 279–288.
- [9] Thorsten Grosch et al. 2006. Fast and robust high dynamic range image generation with camera and object movement. *Vision, Modeling and Visualization, RWTH Aachen 277284*, 3 (2006), 2.
- [10] Shuhang Gu, Yawei Li, Luc Van Gool, and Radu Timofte. 2019. Self-guided network for fast image denoising. In *Proc. Int. Conf. Comput. Vis.* 2511–2520.
- [11] Jin Han, Chu Zhou, Peiqi Duan, Yehui Tang, Chang Xu, Chao Xu, Tiejun Huang, and Boxin Shi. 2020. Neuromorphic camera guided high dynamic range imaging. In *Proc. IEEE Conf. Comput. Vis. Pattern Recog.* 1730–1739.
- [12] Felix Heide, Markus Steinberger, Yun-Ta Tsai, Mushfiqur Rouf, Dawid Pająk, Dikpal Reddy, Orazio Gallo, Jing Liu, Wolfgang Heidrich, Karen Egiazarian, et al. 2014. Flexisp: A flexible camera image processing framework. *ACM Trans. Graph.* 33, 6 (2014), 1–13.
- [13] Yong Seok Heo, Kyoung Mu Lee, Sang Uk Lee, Youngsu Moon, and Joonhyuk Cha. 2010. Ghost-free high dynamic range imaging. In *ACCV*. Springer, 486–500.
- [14] Jun Hu, Orazio Gallo, Kari Pulli, and Xiaobai Sun. 2013. HDR deghosting: How to deal with saturation?. In *Proc. IEEE Conf. Comput. Vis. Pattern Recog.* 1163–1170.
- [15] Katrien Jacobs, Celine Loscos, and Greg Ward. 2008. Automatic high-dynamic range image generation for dynamic scenes. *IEEE Computer Graphics and Applications* 28, 2 (2008), 84–93.
- [16] Nima Khademi Kalantari and Ravi Ramamoorthi. 2019. Deep HDR video from sequences with alternating exposures. In *Comput. Graph. Forum*, Vol. 38. Wiley Online Library, 193–205.
- [17] Nima Khademi Kalantari, Ravi Ramamoorthi, et al. 2017. Deep high dynamic range imaging of dynamic scenes. *ACM Trans. Graph.* 36, 4 (2017), 144–1.
- [18] Nima Khademi Kalantari, Eli Shechtman, Connelly Barnes, Soheil Darabi, Dan B Goldman, and Pradeep Sen. 2013. Patch-based high dynamic range video. *ACM Trans. Graph.* 32, 6 (2013), 202–1.
- [19] Sing Bing Kang, Matthew Uyttendaele, Simon Winder, and Richard Szeliski. 2003. High dynamic range video. *ACM Trans. Graph.* 22, 3 (2003), 319–325.
- [20] Erum Arif Khan, Ahmet Oguz Akyuz, and Erik Reinhard. 2006. Ghost removal in high dynamic range images. In *IEEE Int. Conf. Image Process.* IEEE, 2005–2008.
- [21] Diederik P. Kingma and Jimmy Ba. 2015. Adam: A Method for Stochastic Optimization. *Proc. Int. Conf. Learn. Represent.* abs/1412.6980 (2015). <https://api.semanticscholar.org/CorpusID:6628106>
- [22] Lingtong Kong, Boyuan Jiang, Donghao Luo, Wenqing Chu, Xiaoming Huang, Ying Tai, Chengjie Wang, and Jie Yang. 2022. Ifrnet: Intermediate feature refine network for efficient frame interpolation. In *Proc. IEEE Conf. Comput. Vis. Pattern Recog.* 1969–1978.
- [23] Joel Kronander, Stefan Gustavson, Gerhard Bonnet, and Jonas Unger. 2013. Unified HDR reconstruction from raw CFA data. In *IEEE Int. Conf. Comput. Photo.* IEEE, 1–9.
- [24] Joel Kronander, Stefan Gustavson, Gerhard Bonnet, Anders Ynnerman, and Jonas Unger. 2014. A unified framework for multi-sensor HDR video reconstruction. *Signal Process. Image Commun.* 29, 2 (2014), 203–215.
- [25] Chul Lee, Yuelong Li, and Vishal Monga. 2014. Ghost-free high dynamic range imaging via rank minimization. *IEEE Sign. Process. Letters* 21, 9 (2014), 1045–1049.
- [26] Shuaizheng Liu, Xindong Zhang, Lingchen Sun, Zhetong Liang, Hui Zeng, and Lei Zhang. 2023. Joint hdr denoising and fusion: A real-world mobile hdr image dataset. In *Proc. IEEE Conf. Comput. Vis. Pattern Recog.* 13966–13975.
- [27] Ze Liu, Yutong Lin, Yue Cao, Han Hu, Yixuan Wei, Zheng Zhang, Stephen Lin, and Baining Guo. 2021. Swin transformer: Hierarchical vision transformer using shifted windows. In *Proc. Int. Conf. Comput. Vis.* 10012–10022.
- [28] Zhen Liu, Yinglong Wang, Bing Zeng, and Shuaicheng Liu. 2022. Ghost-free high dynamic range imaging with context-aware transformer. In *Proc. Eur. Conf. Comput. Vis.* Springer, 344–360.
- [29] Kede Ma, Hui Li, Hongwei Yong, Zhou Wang, Deyu Meng, and Lei Zhang. 2017. Robust multi-exposure image fusion: a structural patch decomposition approach. *IEEE Trans. Image Process.* 26, 5 (2017), 2519–2532.
- [30] Stephen Mangiat and Jerry Gibson. 2011. Spatially adaptive filtering for registration artifact removal in HDR video. In *IEEE Int. Conf. Image Process.* IEEE, 1317–1320.
- [31] Rafal Mantiuk, Kil Joong Kim, Allan G Rempel, and Wolfgang Heidrich. 2011. HDR-VDP-2: A calibrated visual metric for visibility and quality predictions in all luminance conditions. *ACM Trans. Graph.* 30, 4 (2011), 1–14.
- [32] Morgan McGuire, Wojciech Matusik, Hanspeter Pfister, Billy Chen, John F Hughes, and Shree K Nayar. 2007. Optical splitting trees for high-precision monocular imaging. *IEEE Comput. Graph. Appl.* 27, 2 (2007), 32–42.
- [33] Simon Meister, Junhwa Hur, and Stefan Roth. 2018. Unflow: Unsupervised learning of optical flow with a bidirectional census loss. In *Proc. of AAAI Conf. Artif. Intell.*, Vol. 32.
- [34] Shree K Nayar and Tomoo Mitsunaga. 2000. High dynamic range imaging: Spatially varying pixel exposures. In *Proc. IEEE Conf. Comput. Vis. Pattern Recog.*, Vol. 1. 472–479.
- [35] Yuzhen Niu, Jianbin Wu, Wenxi Liu, Wenzhong Guo, and Rynson WH Lau. 2021. HDR-GAN: HDR image reconstruction from multi-exposed LDR images with large motions. *IEEE Trans. Image Process.* 30 (2021), 3885–3896.
- [36] Tae-Hyun Oh, Joon-Young Lee, Yu-Wing Tai, and In So Kweon. 2014. Robust high dynamic range imaging by rank minimization. *37, 6* (2014), 1219–1232.
- [37] Zhiyu Pan, Zhiguo Cao, Kewei Wang, Hao Lu, and Weicai Zhong. 2021. TransView: Inside, Outside, and Across the Cropping View Boundaries. In *Proc. Int. Conf. Comput. Vis.* 4218–4227.
- [38] Zhiyu Pan, Yinpeng Chen, Jiale Zhang, Hao Lu, Zhiguo Cao, and Weicai Zhong. 2023. Find Beauty in the Rare: Contrastive Composition Feature Clustering for Nontrivial Cropping Box Regression. *Proc. of AAAI Conf. Artif. Intell.* (2023), 2011–2019.
- [39] K Ram Prabhakar, Gowtham Senthil, Susmit Agrawal, R Venkatesh Babu, and Rama Krishna Sai S Gorthi. 2021. Labeled from unlabeled: Exploiting unlabeled data for few-shot deep hdr deghosting. In *Proc. IEEE Conf. Comput. Vis. Pattern Recog.* 4875–4885.
- [40] Pradeep Sen, Nima Khademi Kalantari, Maziar Yaesoubi, Soheil Darabi, Dan B Goldman, and Eli Shechtman. 2012. Robust patch-based hdr reconstruction of dynamic scenes. *ACM Trans. Graph.* 31, 6 (2012), 203–1.
- [41] Michael D Tocci, Chris Kiser, Nora Tocci, and Pradeep Sen. 2011. A versatile HDR video production system. *ACM Trans. Graph.* 30, 4 (2011), 1–10.
- [42] Shangzhe Wu, Jiarui Xu, Yu-Wing Tai, and Chi-Keung Tang. 2018. Deep high dynamic range imaging with large foreground motions. In *Proc. Eur. Conf. Comput. Vis.* 117–132.
- [43] Gangwei Xu, Yujin Wang, Jinwei Gu, Tianfan Xue, and Xin Yang. 2024. HDRFlow: Real-Time HDR Video Reconstruction with Large Motions. In *Proc. IEEE Conf. Comput. Vis. Pattern Recog.*
- [44] Tianfan Xue, Baian Chen, Jiajun Wu, Donglai Wei, and William T Freeman. 2019. Video enhancement with task-oriented flow. *Int. J. Comput. Vis.* 127 (2019), 1106–1125.
- [45] Qingsen Yan, Weiye Chen, Song Zhang, Yu Zhu, Jinqiu Sun, and Yanning Zhang. 2023. A unified HDR imaging method with pixel and patch level. In *Proc. IEEE Conf. Comput. Vis. Pattern Recog.* 22211–22220.
- [46] Qingsen Yan, Dong Gong, Qinfeng Shi, Anton van den Hengel, Chunhua Shen, Ian Reid, and Yanning Zhang. 2019. Attention-guided network for ghost-free high dynamic range imaging. In *Proc. IEEE Conf. Comput. Vis. Pattern Recog.* 1751–1760.
- [47] Qingsen Yan, Dong Gong, Pingping Zhang, Qinfeng Shi, Jinqiu Sun, Ian Reid, and Yanning Zhang. 2019. Multi-scale dense networks for deep high dynamic range imaging. In *Proc. IEEE Winter Conf. Appl. Comput. Vis.* IEEE, 41–50.
- [48] Qingsen Yan, Lei Zhang, Yu Liu, Yu Zhu, Jinqiu Sun, Qinfeng Shi, and Yanning Zhang. 2020. Deep HDR imaging via a non-local network. *IEEE Trans. Image Process.* 29 (2020), 4308–4322.
- [49] Ramin Zabih and John Woodfill. 1994. Non-parametric local transforms for computing visual correspondence. In *Proc. Eur. Conf. Comput. Vis.* Springer, 151–158.
- [50] Wei Zhang and Wai-Kuen Cham. 2011. Gradient-directed multiexposure composition. *IEEE Trans. Image Process.* 21, 4 (2011), 2318–2323.
- [51] Hang Zhao, Boxin Shi, Christy Fernandez-Cull, Sai-Kit Yeung, and Ramesh Raskar. 2015. Unbounded high dynamic range photography using a modulo camera. In *2015 IEEE International Conference on Computational Photography (ICCP)*. IEEE, 1–10.
- [52] Henning Zimmer, Andrés Bruhn, and Joachim Weickert. 2011. Freehand HDR imaging of moving scenes with simultaneous resolution enhancement. In *Comput. Graph. Forum*, Vol. 30. Wiley Online Library, 405–414.

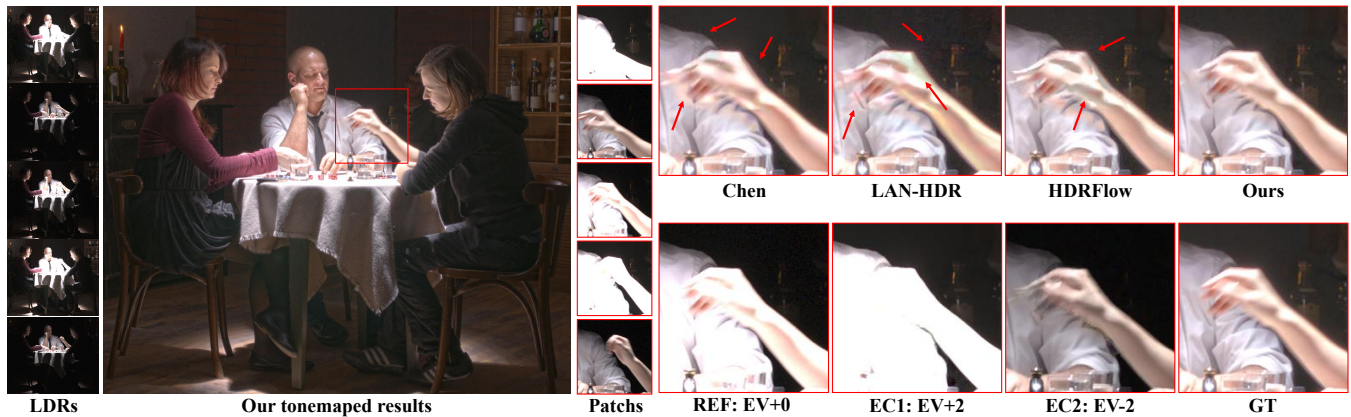


Figure 7: Qualitative comparisons of the three-exposure setting on the Cinematic Video dataset [8]. We compare our proposed method with the current state-of-the-art methods: Chen [3], LAN-HDR [6], HDRFlow [43]. REF refers to reference frame. “EV” refers to the exposure value. “EC1” and “EC2” mean the first and second completed frames with the missing exposure.



Figure 8: Qualitative comparisons of the three-exposure setting on the Cinematic Video dataset [8] and the HDRVideo dataset [18]. EC1 and EC2 mean the first and second completed frames with the missing exposure.

A MORE QUANTITATIVE RESULTS

In Table 4 and Table 5, we provide the results of the current and proposed methods on the more recent metrics under the two-exposure setting, which are all tested on the CinematicVideo dataset [8]. As shown in the Table 4, our method has achieved the state-of-the-art performance on the more recent image quality metrics. We also conduct comparisons on the video quality metric ForVideoVDP in Table 5, which considers information in temporal domain. Our method achieved state-of-the-art performance on this metric also.

Table 4: Additional results on more recent metrics

Methods	HDRVDP3	PSNR _{PU}	SSIM _{PU}	PSNR _{PU} ^{CRF}	SSIM _{PU} ^{CRF}
Chen	9.22	<u>34.24</u>	<u>0.9190</u>	<u>34.45</u>	<u>0.9188</u>
LAN-HDR	9.05	32.30	0.9017	33.11	0.9041
HDRFlow	<u>9.28</u>	33.24	0.9146	33.47	0.9168
Ours	9.30	34.66	0.9292	34.84	0.9290

Table 5: The performance on video metrics: ForVideoVDP

Methods	Chen	LAN-HDR	HDRFlow	Ours
ForVideoVDP	<u>8.9950</u>	8.3404	8.8692	9.0680

Table 6: The efficiency of current and proposed methods

Methods	Flops(G)	Para.(M)	Time(ms)	PSNR _T	SSIM _T
Chen	-	6.1	522	35.65	0.8949
LAN-HDR	3046	7.3	415	38.22	0.9100
HDRFlow	367	3.3	55	39.30	0.9156
Ours	1376	8.8	178	40.59	0.9241

Table 7: Quantitative comparisons with the lightweight version methods “NECHDR-lw”.

	two-Exposures		three-Exposures	
	NECHDR	NECHDR-lw	NECHDR	NECHDR-lw
Para. (M)	8.8	4.2 (↓ 52%)	9.9	4.8 (↓ 52%)
Time (s)	0.178	0.138 (↓ 23%)	0.163	0.130 (↓ 20%)
PSNR _T	40.59	40.33 (↓ 0.7%)	37.24	37.11 (↓ 0.3%)
SSIM _T	0.9241	0.9217 (↓ 0.3%)	0.9102	0.9053 (↓ 0.5%)

B THE EFFICIENCY OF THE PROPOSED METHODS

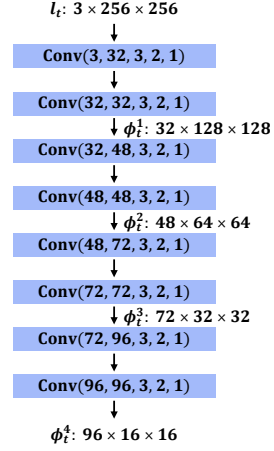
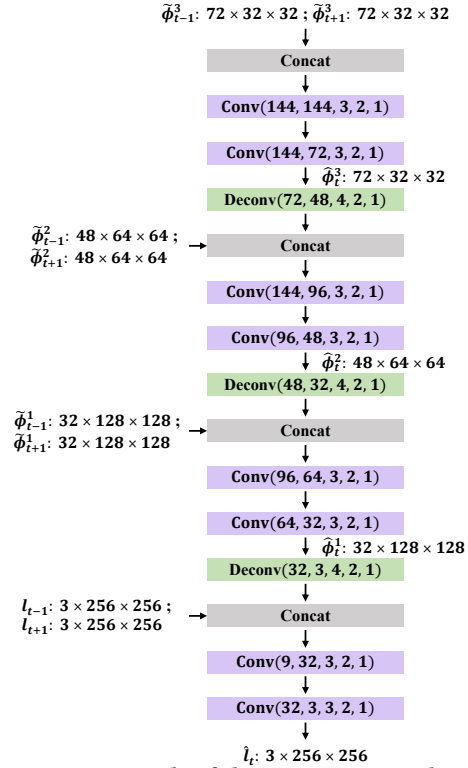
In Table 6, we provide a comparison of the efficiency between our proposed method and the current state-of-the-art methods on the CinematicVideo dataset [8] under the two-exposure setting. In both settings, we offer lightweight versions of the NECHDR network by reducing the number of feature channels. In the lightweight versions, feature channels from the first to the fourth levels in feature encoder \mathcal{E} is set to 24, 36, 54, 72, respectively. The channels of both the exposure completing decoder \mathcal{D}_I and HDR rendering decoder \mathcal{D}_R are adjusted accordingly. Furthermore, the number of feature channels in the third and fifth convolution layers of HDR rendering decoder \mathcal{D}_R will be adjusted to 24. As shown in Table 7, reducing the number of feature channels significantly decreases the parameter and inference time of our model, with no noticeable change in performance.

C THE ABLATION STUDY OF LOSS FUNCTIONS.

The ablation study of the loss functions is provided in Table 8. A significant performance improvement occurs after adding the exposure completion loss \mathcal{L}_I^{com} , which validates our core contribution: the importance of exposure completion for HDR video rendering. The losses for features are introduced in [22] to provide useful low-level structure information. Here, the losses can enhance the details of HDR rendering, thereby improving performance. Finally, combined with optical flow loss \mathcal{L}_F , our method achieves the final performance.

Table 8: The ablation of losses in our method

\mathcal{L}_I^{ren}	\mathcal{L}_I^{com}	\mathcal{L}_G^{ren}	\mathcal{L}_G^{com}	\mathcal{L}_F	PSNR _T	SSIM _T
✓					39.83	0.9213
✓	✓				40.46	0.9225
✓	✓	✓			40.50	0.9231
✓	✓	✓	✓		40.52	0.9932
✓	✓	✓	✓	✓	40.59	0.9941

**Figure 9: Details of the feature encoder \mathcal{E}** **Figure 10: Details of the exposure completing decoder \mathcal{D}_I**

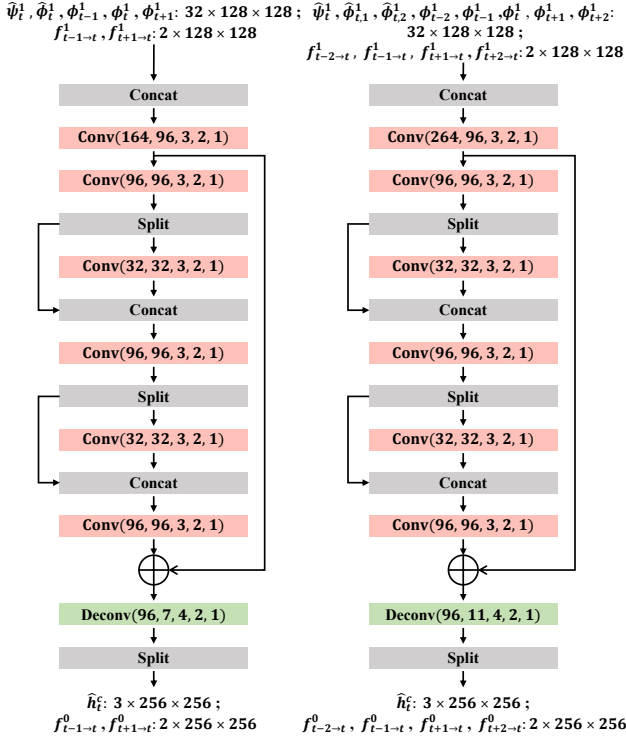


Figure 11: Details of the HDR rendering decoder \mathcal{D}_R^1 . Left: two-exposure; right: three-exposure.

D MORE QUALITATIVE COMPARISONS

Under the three-exposure setting, we provide more qualitative comparison results in Fig. 7 and Fig. 8 between our method and the current state-of-the-art approaches: Chen [3], LAN-HDR [6], HDR-Flow [43]. As shown in Fig. 7, we obtain the completed frames “EC1” and “EC2”. The “EC1” provides high-exposure information with high signal-to-noise ratio to assist in removing noise from the dark background of the reference frame, while “EC2” offers low-exposure foreground object details to restore details missing due to overexposure in the reference frame. Therefore, our proposed method achieves the HDR rendering result closest to ground truth. We also provide two scenarios in Fig. 8, where motions occur with saturation and noise respectively. In the left image of Fig. 8, although “EC1” is not well completed due to the large noise and motion of the first and fourth input frames, the well-completed “EC2” provides information about the saturated regions for HDR rendering, resulting in ghost-free HDR result. In the right image of Fig. 8, the completed frame “EC2” provides detailed information with low noise, thus achieving the lowest noise level in these methods. The above visualization results elucidate the performance enhancement of our method under the three-exposure setting, further proving the robustness of our approach across different exposure settings.

E NETWORK ARCHITECTURE

We provide details of the NECHDR network we proposed, mainly including the following sub-networks: feature encoder \mathcal{E} , exposure completing decoder \mathcal{D}_I , k -levels HDR rendering decoders $\{\mathcal{D}_R^k | k =$

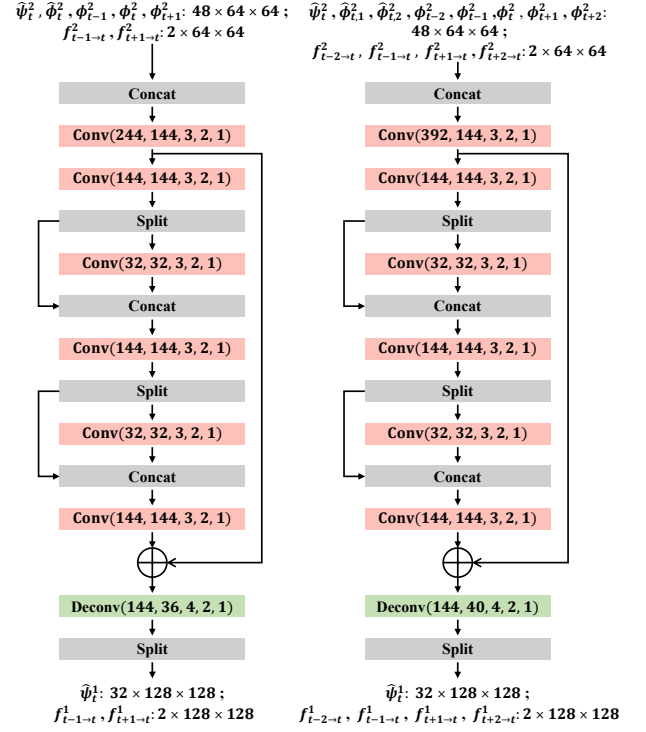


Figure 12: Details of the HDR rendering decoder \mathcal{D}_R^2 .

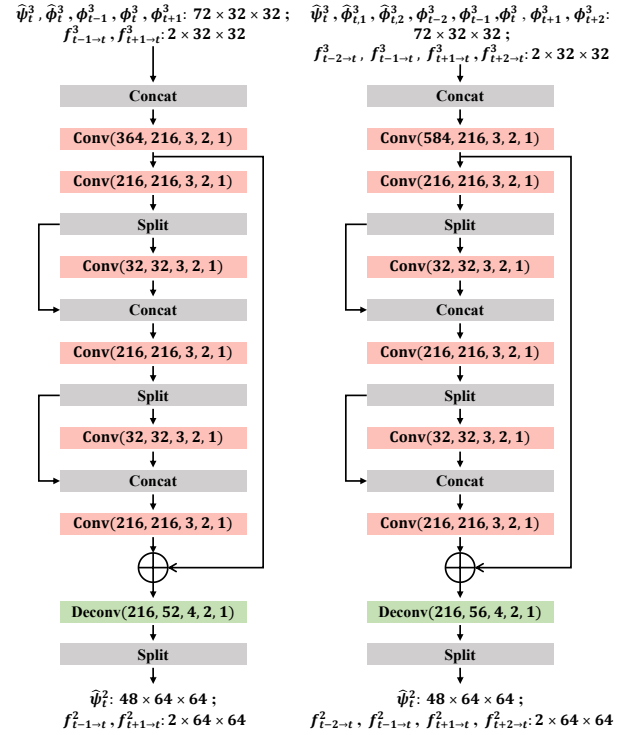
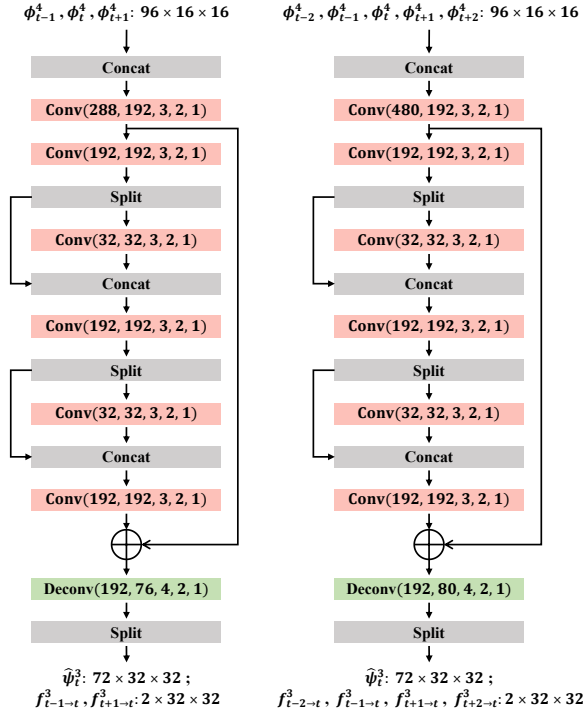


Figure 13: Details of the HDR rendering decoder \mathcal{D}_R^3 .

Figure 14: Details of the HDR rendering decoder \mathcal{D}_R^4 .

1, 2, 3, 4} and blending network. Both The feature encoder \mathcal{E} and exposure-completing decoder \mathcal{D}_I are weight-shared in the two-exposure setting or the three-exposure setting. We take input LDR frames with a size of 256×256 as example and illustrate in figures for above sub-networks. In Fig. 9, 10, 11, 12, 13, 14, the parameters for “Conv” and “Deconv”, listed from left to right, are input channels, output channels, kernel size, stride, and padding. In our network, each “Conv” is followed by a PReLU, whereas there is no activation subsequent to each ‘Deconv’ layer.

In the two-exposure setting, the parameter shared feature encoder \mathcal{E} in Fig. 9 outputs pyramid features for the three input LDR frames $\{l_{t-1}, l_t, l_{t+1}\}$, while for the five input LDR frames $\{l_{t-2}, l_{t-1}, l_t, l_{t+1}, l_{t+2}\}$ in the three-exposure setting. As for the exposure completing decoder \mathcal{D}_I in the Fig. 10, we adopt the same structure and parameters in both settings. Particularly, in the three-exposure setting, the parameter shared decoder \mathcal{D}_I is utilized twice, producing two interpolated frames $\{\hat{l}_t^{c_1}, \hat{l}_t^{c_2}\}$ and their corresponding features $\hat{\Phi}_{t,1}^k = \{\hat{\phi}_{t,1}^k | k = 1, 2, 3\}$, $\hat{\Phi}_{t,2}^k = \{\hat{\phi}_{t,2}^k | k = 1, 2, 3\}$. The details of HDR rendering decoder \mathcal{D}_I^k in k levels, where $k = 1, 2, 3, 4$, are shown in Fig. 11, 12, 13, 14, respectively. In each of the Fig. 11, 12, 13, 14, the left illustrates the k -th level \mathcal{D}_I^k under two-exposure setting, while the right is under three-exposure setting. The details regarding the blending network can be found in [43].